

# Perfect-Lens Theory Enables Metasurface Reflectors for Subwavelength Focusing

Hamidreza Taghvaei<sup>1,3</sup>, Fu Liu<sup>2,\*</sup>, Ana Díaz-Rubio,<sup>3,4</sup> and Sergei Tretyakov<sup>3</sup>

<sup>1</sup>*The George Green Institute for Electromagnetics Research, Faculty of Engineering, University of Nottingham, Nottingham NG7 2RD, United Kingdom*

<sup>2</sup>*Key Laboratory for Physical Electronics and Devices of the Ministry of Education and Shaanxi Key Lab of Information Photonic Technique, School of Electronic Science and Engineering, Faculty of Electronic and Information Engineering, Xi'an Jiaotong University, Xi'an 710049, China*

<sup>3</sup>*Department of Electronics and Nanoengineering, Aalto University, P.O. Box 15500, FI-00076 Aalto, Finland*

<sup>4</sup>*Nanophotonics Technology Center, Universitat Politècnica de València, 46022 Valencia, Spain*



(Received 16 July 2022; revised 31 October 2022; accepted 7 November 2022; published 3 January 2023)

Breaking the so-called diffraction limit on the resolution of optical devices and achieving subwavelength focusing requires tailoring the evanescent spectrum of wave fields. There are several possible approaches, all of which have limitations, such as the generation of strong additional scattering, limited focusing power, issues at the implementation step, and the need for a drain at the focal point. This paper presents a feasible strategy based on the concepts of the perfect lens and power flow-conformal metasurfaces. Desired fields for subwavelength focusing are integrated using double-negative media and then the surface profile of a focusing reflector is designed to be tangential to the desired power flow, so that the metasurface can be modeled as a local impedance boundary, and can be easily implemented using passive and lossless elements. Full-wave simulations demonstrate that an example reactive metasurface is able to break the diffraction limit and provide near-field focusing with subwavelength hotspot size. We expect that the outcome will find applications in antennas, beam-shaping devices, nonradiative wireless power transfer systems, microscopy, and lithography.

DOI: [10.1103/PhysRevApplied.19.014004](https://doi.org/10.1103/PhysRevApplied.19.014004)

## I. INTRODUCTION

Subwavelength focusing is invaluable when it comes to enhancing the resolution of imaging systems, increasing the sensitivity of detectors, and improving numerous other applications, including superresolution microscopy and nanoscopy, nanolithography, and optical trapping. Overcoming the diffraction limit and focusing with subwavelength resolution requires tailoring the evanescent spectrum of an aperture field distribution. Means for shaping electromagnetic near fields have intrigued scientists and engineers since the time when Synge proposed detecting near fields to obtain resolutions beyond the diffraction limit [1]. In 1968, Victor Veselago described electromagnetic properties of materials with simultaneously negative permittivity and permeability and discussed focusing devices that operate based on negative refraction [2]. In 2000, John Pendry showed that a planar slab of a negative refractive index material can manipulate near fields in such a way that perfect imaging can be theoretically achieved, that is, a perfect reconstruction of the near and far field sources [3].

\*fu.liu@xjtu.edu.cn

Following these works, negative refractive index and negative permittivity superlenses have been experimentally verified at microwave, infrared, and optical frequencies [4–7]. In 2007, a related but alternative approach was introduced which relies on patterned, gratinglike surfaces, to obtain subwavelength resolutions [8–11]. These structures, however, can be used only if the object is located in the vicinity of the focusing plate (much smaller than the wavelength). This disadvantage can be overcome with the use of superoscillations [12–14], but at the cost of scattering most of the incident power into parasitic propagating modes. Near-field plates have been designed and demonstrated in homogeneous [15,16] and inhomogeneous [17] media using semianalytical techniques.

Metasurfaces that consist of subwavelength arrays of engineered meta-atoms with tailored electromagnetic properties have provided unprecedented opportunities [18–23]. These functional materials can control the vectorial properties of light waves locally. The local field enhancement has the potential to excite evanescent fields and form subwavelength focal spots [24–32], useful for many applications such as high-resolution sensing and wireless power transfer. Despite the broad variety of methods known to allow subwavelength field concentration and focusing, all

of them have their specific limitations and disadvantages, and it is important to explore other possibilities that may offer complementary advantages and further develop our understanding of these phenomena.

In this paper, we incorporate the principle of power flow-conformal metasurfaces [33–35] with the concept of the perfect lens [3] to design a lossless reflector for enhancing and focusing evanescent waves. Physically, evanescent modes cannot be amplified while propagating, but they can be amplified in resonant structures such as a double-negative slab forming a theoretical perfect lens [3] or a properly designed metasurface [26]. We use the conventional power flow-conformal method to implement subwavelength-focusing reflectors with passive and lossless elements. In Sec. II, we briefly review the power flow-conformal method and outline the scenarios under study. In Sec. III, the theory of forming subwavelength focal spots is explained. Section IV implements the proposed strategy and presents the results. In Sec. V, we investigate the robustness of focusing. Section VI concludes.

## II. FROM POWER FLOW-CONFORMAL ANOMALOUS REFLECTORS TO SUBWAVELENGTH FOCUSING

Before starting with the design of subwavelength focusing reflectors, let us recall the general operating principle of power flow-conformal metasurfaces by analyzing the general reflection scenario. Originally, the power flow-conformal design was proposed to create anomalous reflectors that reflect incident plane waves into plane waves propagating into arbitrary directions [33–35]. To design a reflector using this approach, one first defines the desired field distribution of the incident and reflected waves. For anomalous reflectors, the reflected wave can be considered as created by a virtual plane-wave source behind the reflector. The amplitude of the reflected wave is selected to ensure power conservation in the reflection process.

Based on the uniqueness theorem, the action of the virtual source that creates the desired reflected wave can be replaced by an impedance boundary, with the surface impedance defined by the desired distribution of the total field. For a flat boundary, this impedance is in general complex-valued, corresponding to a locally active or lossy boundary, although the overall response is lossless. This problem can be overcome using power flow-conformal metasurfaces, where the reflecting impedance boundary surface is shaped so that at every point of the boundary the power flow of the desired field distribution is tangential to the boundary. In this case, the required surface impedance is purely reactive everywhere on the reflector surface, and the device can be easily realized using small phase-shifting elements.

In our recent work [36], we have used this power flow-conformal mirror approach to realize subwavelength

focusing, requiring that the desired reflected waves converge to a point (or to a line, in the two-dimensional case). However, in that case, the presence of a drain is required to absorb the power of the focused wave after convergence at the focal point. Even more importantly, in that case, the evanescent fields grow towards the focal point, but that is possible only in the presence of an object that maintains currents. Actually, in this case, the near-field distribution depends on the size and shape of this receiver, and the focus is ideal only if the induced current distribution at the receiving object is the same as that at the transmitting antenna. This means that the realized effect cannot even be considered “imaging.” In fact, this problem is common to several other known approaches to subwavelength focusing [37–41]. This type of drain device can be implemented with active elements where the temporal and spatial properties are controlled [42] or using passive implementations [43,44]. Importantly, the presence of the drain is required for the proper operation of the focusing device.

To overcome this fundamental problem, we need to make sure that after the reflected power is collected at the focal point, this power would continue propagation (diverging again). It is important to stress that in this scenario the evanescent fields decay from the reflector to the focal point. That is, the high-amplitude resonant currents that create focused near fields flow at the reflector surface and not at the focal-point receiver. In this case, subwavelength field energy concentration becomes possible even in free space, in the absence of any receiver or absorber at the focal point. But what virtual source can form this desired field structure?

We explore the possibility of checking that the reflected fields are the same as the fields created by a point source behind a perfect lens (fields are formed by a slab of a double-negative material with relative permittivity and permeability equal to  $-1$ ) [45]. Indeed, between the slab surface and the focal point, the power distribution corresponds to perfect focusing, and behind the focal plane, the fields are the same as those of a point source at the focal point. Thus, the reflected power passes through the focus and continues propagation in space towards infinity. This is exactly the field structure required for a perfectly focusing reflector. This scenario is illustrated in Figs. 1(a) and 1(b). In usual parabolic reflectors, the reflected wave, shown by yellow arrows, converges to the focal point as a diffraction-limited beam. The aim is the creation of a reflector whose reflected waves behave as a perfectly focusing beam created by a virtual source behind a perfect lens.

To do that, we can replace the virtual source and the perfect lens with a reflecting boundary, setting its surface impedance to the ratio of the tangential electric and magnetic fields at the reflector surface, as illustrated in Fig. 1(c). For a flat reflector, this impedance is complex-valued, but the overall response can be made lossless by

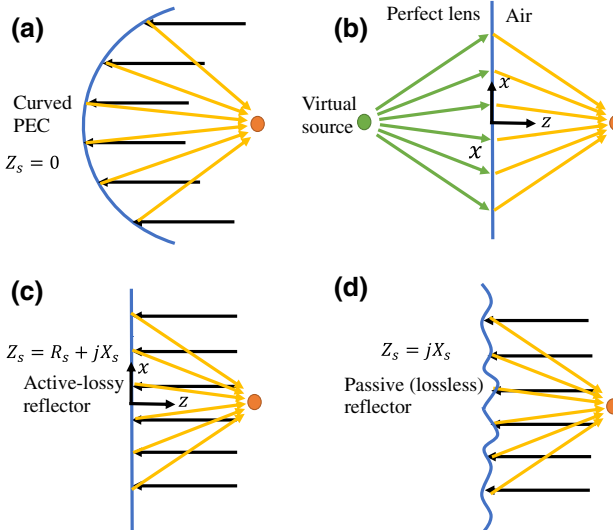


FIG. 1. Power flow-conformal focusing. (a) Simple diffraction-limited curved (parabolic) perfect electric conductor (PEC) reflector designed for focusing. (b) Virtual source behind a perfect lens formed by double-negative medium slab. Using the total field, we can calculate the required surface impedance of the subwavelength-focusing reflector. (c) A flat focusing reflector is implemented as an “active-lossy” metasurface. (d) “Passive (lossless)” power flow-conformal focusing reflector.

adjusting the amplitude of the virtual source so that the wave structure formed satisfies energy conservation and the total power crossing the reflector plane is zero. Still, for a flat reflector, the required surface impedance remains complex-valued, with some areas being active and some areas being lossy.

Finally, the reflector can be shaped following the principle of power flow-conformal metasurfaces so that the reflecting surface is tangential to the desired distribution of the Poynting vector. In this case, the surface impedance of the metasurface is purely imaginary at all points, and the surface can be implemented using simple lossless meta-atoms. This solution is schematically illustrated in Fig. 1(d).

### III. ENGINEERING EVANESCENT WAVES FOR PERFECT IMAGE

We start by writing analytical expressions for the desired total field in front of the reflector. This field is the sum of the incident field and the field created by the virtual source behind the perfect lens. For simplicity, we consider a two-dimensional problem where the virtual source is an infinite current line along the  $y$  axis. Figure 2 displays the setup of the model under study. A perfect lens made of a medium with relative permittivity and permeability  $\epsilon_r = \mu_r = -1$  is in the region  $-d < z < 0$  in free space, while the virtual source is located at  $(z_s, x_s) = (-d, 0)$  behind

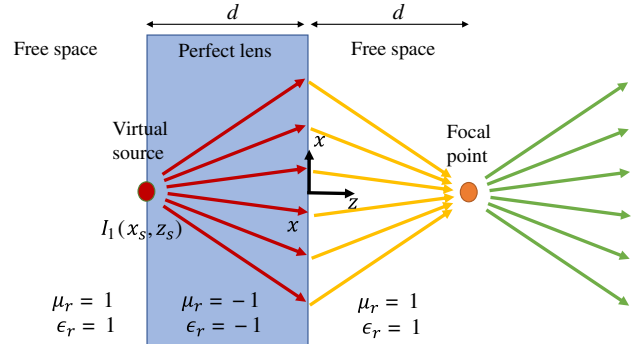


FIG. 2. The virtual source behind the perfect lens as a double-negative medium. Diverging-amplifying fields inside the lens and converging-decaying fields outside the lens help us to calculate the desired total field and hence the required surface impedance.

the perfect lens. The perfect lens is used to amplify the evanescent modes of the virtual source field and then construct the perfect image at the focal point at  $(z, x) = (d, 0)$ . In this way, the fields in the region  $z > 0$  are our desired reflected field for deeply subwavelength focusing in reflection.

The virtual source, placed in the air just at the interface with the perfect lens, is an infinitesimally thin current line supporting a uniform current  $I_1$ . The incident electric and magnetic fields created by this source (e.g., [46]) are given by

$$\mathbf{E}_s = E_s \hat{y} = -\frac{\eta k I_1}{4} H_0^{(2)}(kr_s) \hat{y}, \quad \mathbf{H}_s = \frac{j}{\eta k} \nabla \times \mathbf{E}_s, \quad (1)$$

where the subscript  $s$  marks the source fields,  $\eta$  is the free-space impedance,  $k$  is the vacuum wave number at the operation frequency,  $I_1$  is the amplitude of the virtual source current,  $H_0^{(2)}$  is the zeroth-order Hankel function of the second kind with  $r_s = |\mathbf{r} - \mathbf{r}_s| = \sqrt{(z - z_s)^2 + (x - x_s)^2}$  being the distance from the observation point  $\mathbf{r} = (z, x)$  to the current location  $\mathbf{r}_s = (z_s, x_s)$ , and  $\hat{y}$  is the unit vector in the  $y$  direction. A harmonic time dependence of the form  $\exp(j\omega t)$  is assumed. Because the perfect lens is matched and does not introduce any reflections, this cylindrical wave is the total field created by the virtual source in front of the lens.

To study the distribution of the desired field, we consider the propagation of spatial Fourier harmonics (including propagating and evanescent modes) of the source field inside the perfect lens in the region  $-d < z < 0$  and then in free space in the region  $z > 0$ . Firstly, at the source position  $z = -d$ , the complex amplitudes of the spatial harmonics in terms of  $k_x$  are obtained by the Fourier transform of

Eq. (1), and they are given by

$$\mathcal{F}(E_s)|_{z=-d} = -\frac{\eta k I_1}{4} \frac{2}{\sqrt{k^2 - k_x^2}}, \quad (2)$$

with the choice of the square root branch

$$\text{Im} \left( \sqrt{k^2 - k_x^2} \right) < 0. \quad (3)$$

Then, inside the perfect lens region  $-d < z < 0$ , all of these harmonic modes evolve with  $e^{j\sqrt{k^2 - k_x^2}(z+d)}$ , which means that the evanescent modes with  $k_x > k$  are amplified while the propagation modes with  $k_x < k$  propagate with a negative phase velocity. As a result, the complex amplitudes of the spatial harmonics at the right-hand side of the perfect lens (i.e., at  $z = 0$ ) become

$$\mathcal{F}(E_s)|_{z=0} = -\frac{\eta k I_1}{4} \frac{2}{\sqrt{k^2 - k_x^2}} e^{j\sqrt{k^2 - k_x^2}d}, \quad (4)$$

where the branch choice of Eq. (3) is again applied. These plane-wave modes continue to propagate in free space in the region  $z > 0$ , but evolve with  $e^{-j\sqrt{k^2 - k_x^2}z}$ , meaning that the evanescent modes with  $k_x > k$  decay in free space. Thus, the amplitudes of spatial harmonics for desired fields in the region  $z > 0$  are given by

$$\mathcal{F}(E_s)|_{z>0} = -\frac{\eta k I_1}{4} \frac{2}{\sqrt{k^2 - k_x^2}} e^{j\sqrt{k^2 - k_x^2}(d-z)}, \quad (5)$$

with the condition of Eq. (3). It is obvious that, at  $z = d$ , the amplitudes of the spatial harmonics are exactly equal to those at the source position  $z = -d$  in Eq. (2). Therefore, perfect focusing can be theoretically achieved.

In Fig. 3 we plot the amplitude of the normalized Fourier spectra in Eqs. (4) and (5) behind the lens ( $z = 0$ ) and around the focal point ( $z = 0.1\lambda$ ), with the thickness of the lens being  $d = 0.2\lambda$ . As we can see, for the fields closer to the focal point, the propagating Fourier components (corresponding to  $|k_x/k| < 1$ ) have the same amplitude, while the evanescent modes (corresponding to  $|k_x/k| > 1$ ) decay quickly, and much more quickly for larger  $|k_x/k|$ . Finally, the desired electric fields in the region  $z > 0$  as functions of coordinates  $z$  and  $x$  are obtained by integrating these spatial harmonics using an inverse Fourier transform:

$$E_y = \frac{1}{2\pi} \int_{-\infty}^{+\infty} (\mathcal{F}(E_s)|_{z>0}) e^{jk_x x} dk_x. \quad (6)$$

Theoretically, the integration should be from  $-\infty$  to  $\infty$  to include the contributions of all spatial harmonics. However, if all spatial harmonics are included, the integral

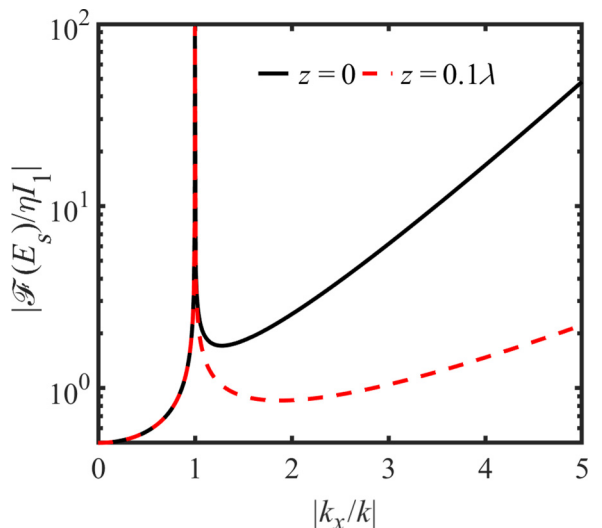


FIG. 3. Normalized Fourier components versus normalized tangential wave number  $k_x/k$  around the focal point at  $z = 0$  and  $z = 0.1\lambda$ . For  $k_x > k$  (evanescent modes) by increasing the  $k_x$  the electric field gets stronger, and when moving away from the lens the evanescent field decays.

diverges everywhere between the focal point and the lens (e.g., [46]) because at the perfect image of a line source the field is singular, and the evanescent fields grow from this point towards the resonant surface of the lens. For waves in free space, the evanescent modes, that is, the modes with the tangential wave number  $k_x > k$ , always decay exponentially from the source while the propagation modes ( $k_x \leq k$ ) propagate. Therefore, for the usual focusing devices, only propagating modes contribute to the focusing but not the evanescent modes. This is the physical reason for the diffraction limit of focusing. The creation of theoretically perfect images by a negative-index slab lens is based on resonant excitation of surface modes with all  $k_x > k$  at the back of the slab lens. The amplitudes of these modes at the lens surface grow exponentially with increasing values of the tangential wavenumbers  $k_x$ , which compensates for the increasing decay factor of the fields created by the corresponding equivalent surface currents. Obviously, perfect imaging requires infinite stored reactive energy and infinite quality factor of these resonant modes. In addition, high-order spatial harmonics vary rapidly along the  $x$ -direction and require very fine spatial sampling of the reflector. Thus, the wavenumbers of the supported resonant modes should be limited. Only in this case do practical realizations of the metasurface device become possible.

Therefore, we trim the integration up to a certain  $k_x$  value,  $k_{\max}(> k)$ , to calculate the desired fields and define the required lens impedance. We note that the desired magnetic fields in the region  $z > 0$  can be obtained in the same way as discussed above. In summary, the expressions for

the desired electric and magnetic fields in the region  $z > 0$ , which are the fields of the virtual source after passing through the perfect lens, are

$$E_y = -\frac{\eta k I_1}{8\pi} \int_{-k_{\max}}^{+k_{\max}} \frac{2}{\sqrt{k^2 - k_x^2}} \Psi(k_x) dk_x, \quad (7)$$

$$H_x = \frac{I_1}{4\pi} \int_{-k_{\max}}^{+k_{\max}} \Psi(k_x) dk_x, \quad (8)$$

$$H_z = \frac{I_1}{4\pi} \int_{-k_{\max}}^{+k_{\max}} \frac{k_x}{\sqrt{k^2 - k_x^2}} \Psi(k_x) dk_x, \quad (9)$$

with  $\Psi(k_x) = e^{-j\sqrt{k^2 - k_x^2}(z-d)} e^{jk_x x}$  and the condition in Eq. (3).

Figure 4 shows the electric field distributions for lenses that support surface modes with tangential wavenumbers  $k_x$  only up to a fixed maximum value  $k_{\max}$ . The focal distance of this lens is  $d = 0.2\lambda$ . Figure 4(a) corresponds to the case when no evanescent modes are contributing, which corresponds to the usual diffraction-limited focusing. Figures 4(b) and 4(c) illustrate subwavelength improvements of focusing due to the excitation of evanescent modes. In Fig. 5 we plot the  $|E_y|^2$  distributions along a line crossing the focal point (i.e., at  $z = d$ ), for considering different ranges of excited evanescent modes. When only the propagating modes contribute to focusing (i.e.,  $k_{\max} = k$ ), the half-power focal size is about  $0.36\lambda$  (see the black line). However, when the evanescent modes up to  $k_{\max} = 2k$  ( $5k$ ) contribute, the half-power focal size shrinks to  $0.26\lambda$  ( $0.14\lambda$ ), much smaller than the case when only propagation modes are contributing (see the dashed red and dotted blue lines), overcoming the diffraction limit. We conclude that excitation of modes even with moderately fast variations over the slab lens surface allows significant improvement of focusing.

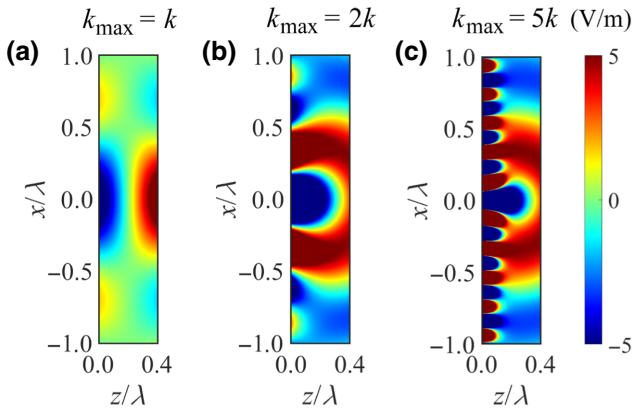


FIG. 4. Imaginary part of the electric field pattern close to the focusing point, when accounting for evanescent modes with  $|k_x| < k_{\max}$ . Subfigures correspond to  $k_{\max} = k$ ,  $2k$ , and  $5k$ , respectively.

Based on this discussion, we select the required field structure of the reflected field as the field behind the perfect lens including evanescent modes with the tangential wavenumbers only up to a certain value of  $k_{\max}$ . When the desired fields have been defined, we can find a corresponding reflector that creates these fields. In the following, we show two methods: one is a flat surface that is active-lossy, and a curved reflecting surface (power flow-conformal metasurface) that is purely reactive, that is, the surface is a lossless reflector at every point.

#### IV. IMPLEMENTATION OF SUBWAVELENGTH FOCUSING IN REFLECTION

As follows from the uniqueness theorem (see also [34,35,47–49]), an impenetrable boundary, defined by the impedance boundary condition

$$\mathbf{E}_t = \mathbf{E}_i + E_y \hat{\mathbf{y}}, \quad (10)$$

$$\mathbf{E}_t = Z_s \hat{\mathbf{n}} \times \mathbf{H}_t, \quad (11)$$

where  $\mathbf{E}_t$  and  $\mathbf{H}_t$  are the total electric and magnetic fields, and  $\hat{\mathbf{n}}$  is the normal unit vector of the surface pointing towards the incident wave source, acts as a reflector creating the desired reflected fields. The total field is the sum of the incident field  $\mathbf{E}_i$  and the field  $E_y \hat{\mathbf{y}}$  created by the virtual source that we discussed above.

The amplitude of the virtual source  $I_1$  should be selected so that the incident power of the illuminating source  $I_0$  is balanced with the power reflected from the metasurface. In this case, the reflector is lossless overall, as the total incident power is equal to the total reflected power. The virtual source amplitude  $I_1$  is adjusted such that the power balance is satisfied at the reflector plane  $z = 0$ . This can be done approximately using the ray model, as is illustrated in Fig. 6. A simple calculation shows that when  $I_1$  is at  $(z_s, x_s) = (-0.2\lambda, 0)$  and the incident current line source  $I_0$  is at  $(z, x) = (10\lambda, 0)$ , we have  $\theta_1 = 90^\circ$  and  $\theta_2 = 177.7^\circ$ .

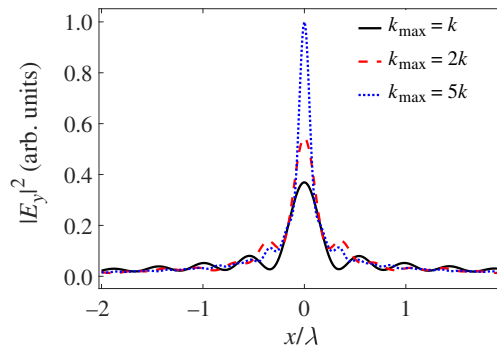


FIG. 5.  $|E_y|^2$  distribution along  $z = d$  crossing the focal point when accounting for evanescent modes. Stronger focused field and narrower hotspot size with higher contribution of evanescent modes.

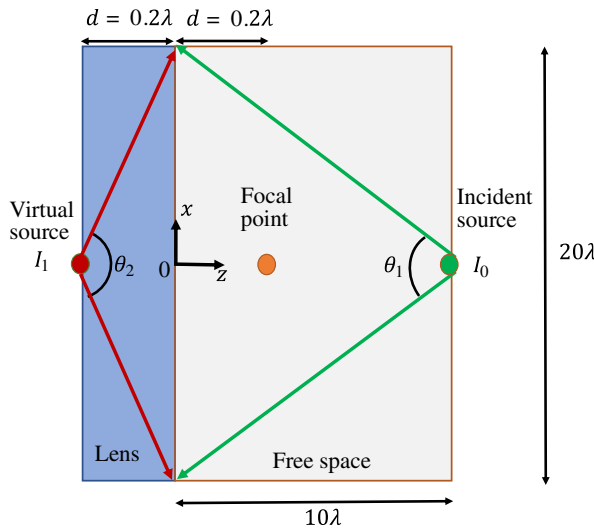


FIG. 6. Schematic of the simulation setup (the geometry is not proportional to the real dimensions): the virtual current line source  $I_1$  is at  $(z_s, x_s) = (-0.2\lambda, 0)$ , the perfect lens occupies  $z \in [-0.2\lambda, 0]$  and  $x \in [-10\lambda, 10\lambda]$ , the focal point is at  $(z, x) = (0.2\lambda, 0)$ , and the illuminating current line source  $I_0$  is at  $(z, x) = (10\lambda, 0)$ .

In this case, the power balance condition is approximately satisfied when  $I_1 = I_0/\sqrt{2}$ .

Figure 7 shows the real and imaginary parts of the electric and magnetic fields calculated by the integration of spatial harmonics. We see that the evanescent fields have high amplitudes at the reflector plane and decay towards the focal point. Since the selected focal distance is small,  $0.2\lambda$ , their amplitudes are enough to ensure strong subwavelength field concentration at the focal point. As discussed above, this property allows deep subwavelength focusing in free space, in the absence of any object at the

focal point. To find the required surface impedance, it is necessary to calculate the tangential components of the magnetic field at each point of the reflector surface.

### A. Flat active-lossy surface implementation

In general, we can select any position and shape of a surface and find the required surface impedance at this surface using Eq. (11). The simplest choice is a flat surface along the  $x$ -direction at the  $z = 0$  plane. As shown in Fig. 8(a), the surface impedance, in this case, is a complex value whose real part takes positive and negative values, meaning that the metasurface locally produces losses or gains. The local gain and loss introduced by the metasurface can be evaluated using the normal vector to the surface component of the Poynting vector. The electric and magnetic fields reflected back from the flat active-lossy surface are plotted in Fig. 9. The fields are almost identical to the desired fields created by the virtual source behind the perfect lens (compare with Fig. 7), with the addition of fast variations on the  $\text{Re}(E_y)$  and  $\text{Im}(\eta H)$  fields close to the metasurface. The absolute value of the reflected power  $P_r = (1/2\eta)|E_r|^2$  ( $\text{W/m}^2$ ) is shown in Fig. 8(b). The hotspot size is a bit larger than  $\lambda/8$ . Although the performance of the subwavelength focusing is excellent, the implementation of active-lossy metasurfaces is obviously not practical. Furthermore, the required surface impedance shows considerable fluctuation and has sharp changes which make it even less feasible.

### B. Flat lossless surface implementation

To allow a practical design, we can simply avoid active-lossy elements by forcing the real part of the surface impedance to be zero and keeping the required imaginary part unchanged. Figure 10(a) shows the surface impedance

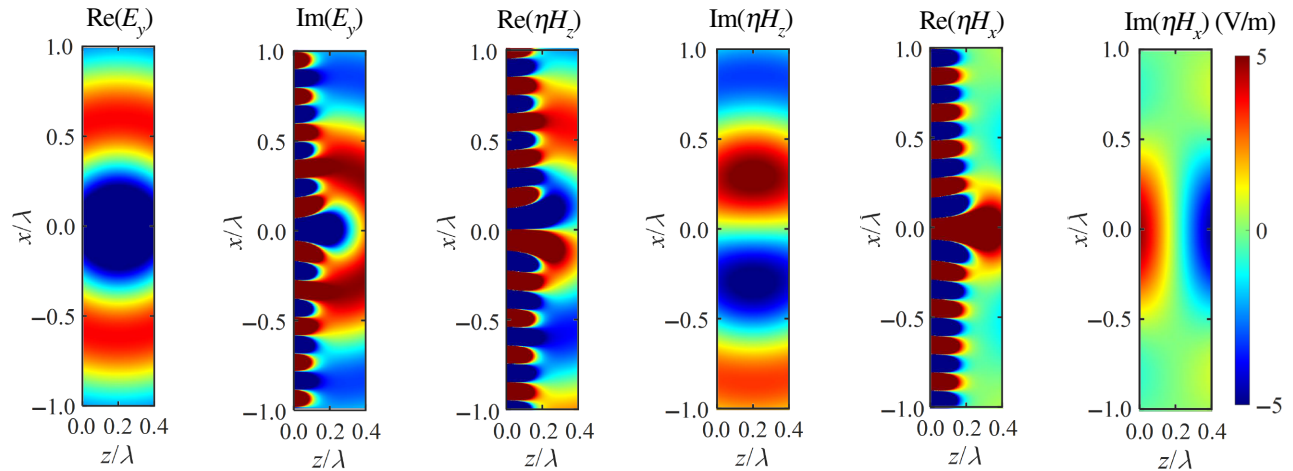


FIG. 7. Real and imaginary parts of the electric and the magnetic fields found using the perfect-lens equation. These fields are created by the virtual source at  $(z_s, x_s) = (-0.2\lambda, 0)$  with  $I_1 = 0.48$  mA at  $F = 10$  GHz and focused at  $(z, x) = (0.2\lambda, 0)$ . Behind the focal plane (i.e., at  $z > 0.2\lambda$ ), the focused field again diverges like a semicylindrical wave.

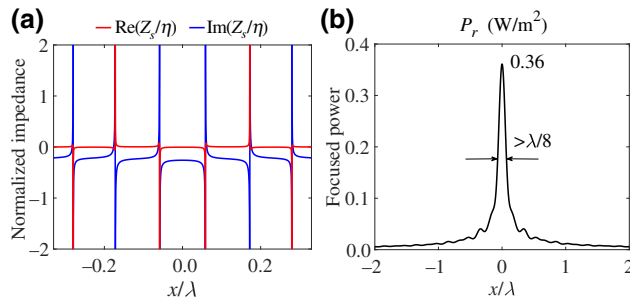


FIG. 8. Electromagnetic properties of an active-lossy flat metasurface along the  $x$ -direction at the  $z = 0$  plane. (a) The surface impedance at the reflecting boundaries  $z = 0$  shows considerable fluctuation with sharp changes. (b) The reflected power at the focal line  $z = 0.2\lambda$  shows focused power  $0.36$  ( $\text{W}/\text{m}^2$ ) and hotspot size more than  $\lambda/8$ .

of such a flat lossless metasurface, and Fig. 10(b) shows the corresponding absolute values of the reflected power. Compared to the active-lossy case, the focused power has declined, but the hotspot size is smaller. With this strategy one can achieve subwavelength focusing, albeit with limited power with lossless elements. Nevertheless, the considerable fluctuation and sharp changes of surface impedance are still an issue. Also, side lobes appear to be stronger, which might be problematic in some cases. The electric and magnetic fields reflected back from the flat lossless surface are plotted in Fig. 11. The fields resemble a weaker version of the fields shown in Fig. 9.

### C. Power flow-conformal surface implementation

A better strategy is to shape the surface with respect to the desired power flow. In this case, the metasurfaces are power flow-conformal, and the

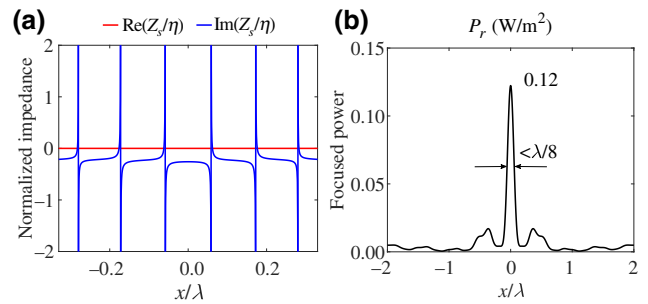


FIG. 10. Electromagnetic properties of a flat lossless metasurface along the  $x$ -direction at the  $z = 0$  plane. (a) The surface impedance at the flat surface  $z = 0$  shows considerable fluctuation and sharp changes. (b) The reflected power at the focal line  $z = 0.2\lambda$  shows focused power  $0.12$  ( $\text{W}/\text{m}^2$ ) and hotspot size less than  $\lambda/8$ .

Poynting vector of total fields is tangential to the surface. Hence, the real part of the surface impedance is identically zero, and the corresponding reflector is lossless at all points.

To this end, we define a vector perpendicular to the Poynting vector as  $\mathbf{N} = -S_x \hat{z} + S_z \hat{x}$  and, using the properties of the gradient, we look for a function  $g(z, x)$  such that  $\nabla g(z, x) = \mathbf{N}$ . This expression resembles the well-known formula for the electric potential in electrostatics,  $\mathbf{E} = -\nabla V$ . Using this mathematical analogy, we calculate  $g(z, x)$  using an electrostatic solver in COMSOL Multiphysics. By defining the electric displacement field to be proportional to vector  $\mathbf{N}$ , we solve the electric potential that is equivalent to the function  $g(z, x)$  (see Fig. 12). Finally, the profile of the power flow-conformal metasurface can be defined as an equipotential surface. There are infinitely many surfaces tangential to the power flow

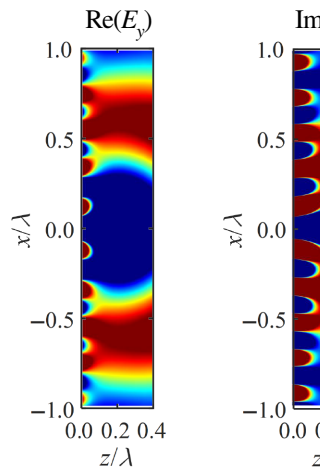


FIG. 9. Real and imaginary parts of the electric and the magnetic fields reflected from the flat active-lossy metasurfaces to focus the reflected fields at  $(z, x) = (0.2\lambda, 0)$ . The incident fields are imposed by the current line source at  $(z, x) = (10\lambda, 0)$  with  $I_0 = 0.48\sqrt{2}$  mA (power balanced) at  $F = 10$  GHz.

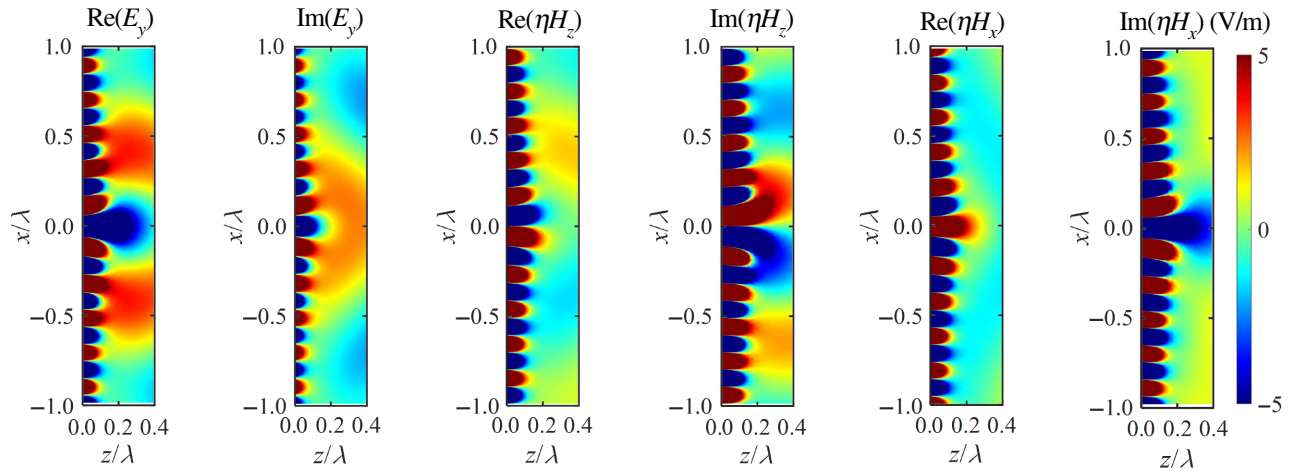


FIG. 11. Real and imaginary parts of the electric and magnetic fields reflected from the flat lossless metasurface to focus the reflected fields at  $(z, x) = (0.2\lambda, 0)$ . The incident fields are imposed by the current line source at  $(z, x) = (10\lambda, 0)$  with  $I_0 = 0.48\sqrt{2}$  mA (power balanced) at  $F = 10$  GHz.

field, and each of them defines a different metasurface with different electromagnetic properties. Black lines in Fig. 12(b) graphically represent a set of conformal surfaces that are tangential to the Poynting vector of the desired field distribution.

To engineer a metasurface based on this analysis, we select one of the conformal lines [see Fig. 12(c)] and calculate the surface impedance defined by Eq. (11). There are some small gaps in the selected surface that we fill with lossless elements by dropping the real part of the required impedance. Figure 13 shows the surface impedance for the selected conformal surface (blue color). The surface impedance is symmetric with respect to the  $x$ -axis. The real part of the surface impedance is zero, indicating the

local and lossless response of the metasurface. The imaginary part of the impedance shows smooth fluctuations of the reactance, responsible for subwavelength wavefront engineering.

Electric and magnetic fields reflected from the conformal surface are plotted in Fig. 14. The fields are stronger than in the flat lossless case (see Fig. 11). Figure 13(a) shows the surface impedance of a conformal metasurface, and Fig. 13(b) shows the corresponding absolute values of the reflected power at the focal line  $z = 0.2\lambda$ . Compared to the flat lossless case, the focused power has increased, but the hotspot size is not changed. Compared to the active-lossy case, the focused power is slightly mitigated, but the hotspot size is smaller. We can conclude that shaping metasurfaces with respect to the power flow allows subwavelength focusing with a high ratio of focused power. Note

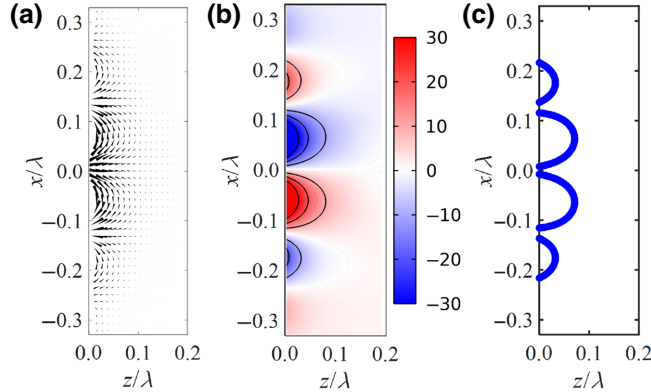


FIG. 12. (a) Poynting vector (represented by the black cones). (b) Electrostatic study to find the shape of power-conformal surfaces. Black lines represent sets of conformal surfaces that are tangential to the Poynting vector. (c) Selected conformal surface where gaps are filled with lossless elements.

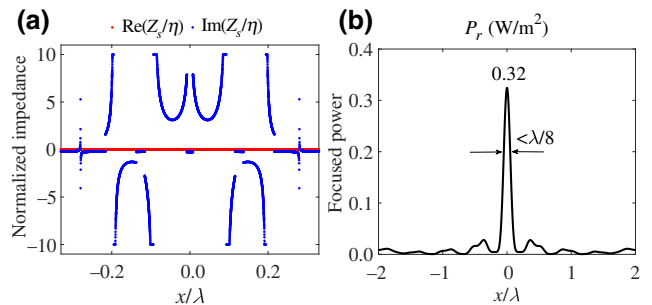


FIG. 13. Electromagnetic properties of a power-flow conformal metasurface along the  $x$ -direction at the  $z = 0$  plane. (a) The surface impedance at the conformal surface shows smooth change. (b) The reflected power at the focal line  $z = 0.2\lambda$  shows focused power  $0.32$  ( $\text{W}/\text{m}^2$ ) and hotspot size less than  $\lambda/8$ .

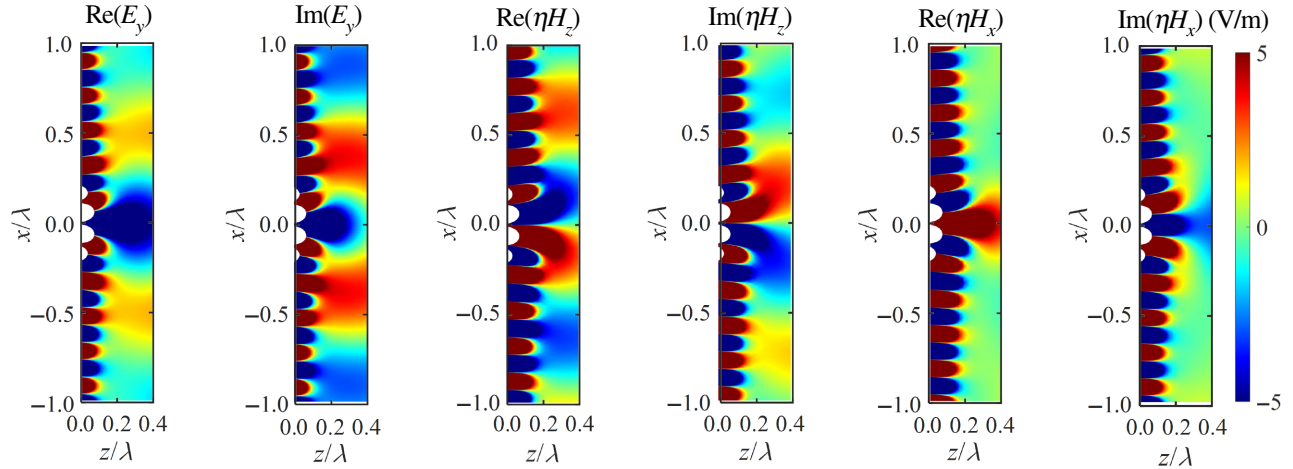


FIG. 14. Real and imaginary parts of the electric and the magnetic fields reflected from the conformal metasurface to focus the reflected fields at  $(z, x) = (0.2\lambda, 0)$ . The incident fields are imposed by the current line source at  $(z, x) = (10\lambda, 0)$  with  $I_0 = 0.48\sqrt{2}$  mA (power balanced) at  $F = 10$  GHz.

also the significantly smoother variations of the required surface reactance along the reflecting surface.

## V. DISCUSSION

In this section, we discuss the peculiarities and advantages of the proposed method for subwavelength focusing. Typically, subwavelength devices are sensitive to changes after deployment. For instance, a displacement of the source can completely compromise the quality of focusing. In contrast, the proposed design is reasonably resilient against source displacement. Figure 15 shows the impact of source position shifts (parallel to the  $x$  axis) on the hotspot size and focused power. The hotspot size is almost unchanged up to  $\lambda/2$  of source displacement. The focused power is not very sensitive either, such that with a  $\lambda/4$  displacement of the source, the focused power decreases by only 16%.

Another important parameter of the reflector is the frequency bandwidth. To study this effect, we introduce the surface inductance  $L$  and capacitance  $C$  of required meta-atoms using relations  $Z_s = j\omega L$  or  $Z_s = 1/(j\omega C)$ , where  $\omega = 2\pi F$  is the design frequency. Figure 16(a) shows the values of the equivalent circuit elements corresponding to the surface impedance profile shown in Fig. 13. These values show smooth change for inductance ranging from 10 to 60 nH and for capacitance ranging from 0.1 to 4 pF.

There are several possibilities for realizing such surface impedance in practice. From microwave to terahertz ranges, it is possible to use basic barlike metasurface units, which have a simple geometry that is easy to optimize. The required surface impedance can be discretized and realized with length and/or width optimization with respect to different reflection phase [50]. Also, one can use the classical high-impedance surface [51,52]. However, since

we need local response, corrugated surfaces are better and even simpler than other solutions. One should only engineer the groove depth  $h$  needed for a specific value of the surface impedance (e.g., [53]),

$$Z_s(x) = j \frac{w}{P} \eta_g \tan[k_g h(x)], \quad (12)$$

where  $h(x)$  is the groove depth,  $\eta_g$  and  $k_g$  are the impedance and wave number in the material filling the grooves,  $w$  is the groove width, and  $P$  is the corrugation period.

The size of the elements  $P$  defines the impedance discretization in the implementation and affects the focusing performance. Figure 17 shows the relationship between the size of the elements and the hotspot size, indicating that up to the  $\lambda_m/25$  discretization step the focusing remains subwavelength.  $\lambda_m$  is the minimal wavelength corresponding to  $k_{\max} = 5k$ .

Next, we study the designed metasurface numerically at frequencies close to the frequency of operation using

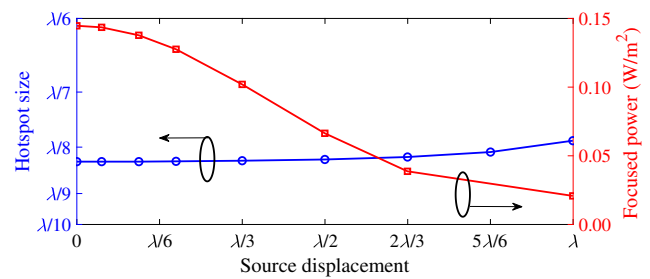


FIG. 15. The hotspot size is resilient against source displacements up to  $0.5\lambda$  displacement. Also, the focused power is not very sensitive up to  $0.25\lambda$  source movements, but beyond that it starts to decline.

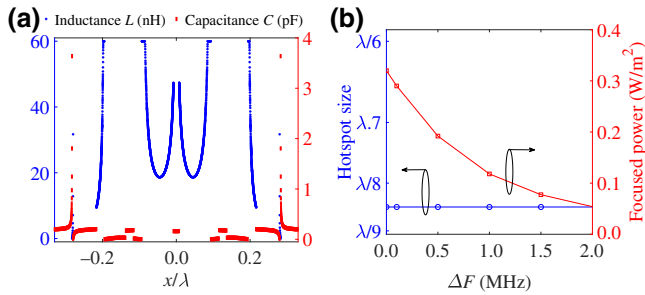


FIG. 16. (a) Values of the inductance and capacitance of the effective circuit elements of the power flow-conformal metasurface. (b) Hotspot size and focused power versus the frequency deviation.

the above relations for surface impedances with the corresponding surface inductance and capacitance. The effects of the frequency dispersion of the surface impedance on the hotspot size and focused power versus the frequency deviation are shown in Fig. 16(b). While the hotspot size appears to be stable, the focused power is rather sensitive to frequency changes. The operational bandwidth is quite narrow such that the focused power is halved at 0.75 MHz away from the central frequency (10 GHz). The reason is partly in the dispersion effect, but mainly it is due to the fact that the power flow distribution depends on the frequency. Thus, when the frequency changes, the Poynting vector field and consequently the position of the tangential surfaces change. Since subwavelength focusing is subject to the careful establishment of power flow-conformal surfaces, significant frequency deviations deteriorate the reflector performance in terms of the collected power. We note also that although most of the meta-atoms are not resonant, the whole metasurface is necessarily resonant, which is the mechanism of evanescent field enhancement.

In the last study, we checked a possibility of subwavelength resolution of two closely positioned sources. Two virtual sources were placed at  $x = \pm\lambda/8$  and  $z = -d$ , corresponding to two actual illumination sources at  $x = \pm\lambda/8$  and  $z = 10\lambda$ . Then we integrated the fields and repeated

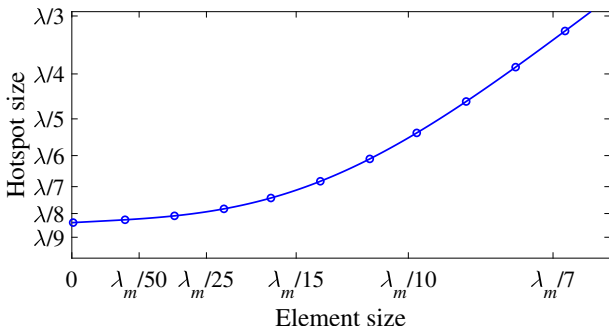


FIG. 17. The hotspot size is almost unchanged for elements size  $P$  smaller than  $\lambda_m/25$ .

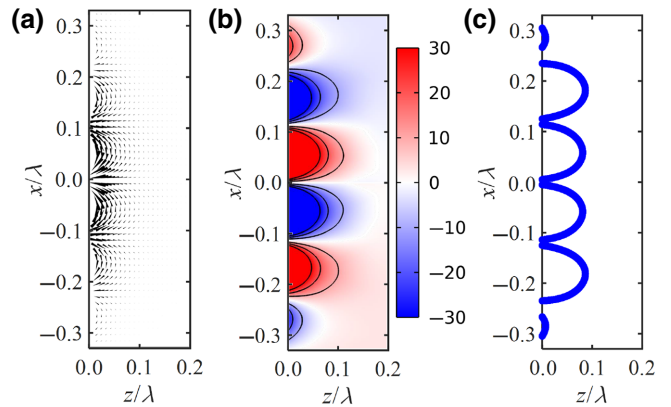


FIG. 18. (a) Poynting vector (represented by the black cones). (b) Electrostatic study to find the shape of power-conformal surfaces. Black lines represent sets of conformal surfaces tangential to the Poynting vector. (c) Selected conformal surface for dual focusing where gaps are filled with lossless elements.

the electrostatic study to find a power flow-conformal surface for dual focal point focusing. Figure 18 shows the Poynting vector (a), the results of the electrostatic analysis with equipotential surfaces (black lines) tangential to the Poynting vectors (b), and the selected conformal surface (c).

Figure 19 shows the complex surface impedance for the selected conformal surface (blue color), where the real part of the impedance is zero  $\text{Re}(Z_s/\eta) = 0$ . The imaginary part at the conformal surface fluctuates rapidly, while the imaginary parts of the gaps filled with lossless elements are almost uniform. The hotspot size is about  $\lambda/9$ . Since we have two sources of the same amplitude, compared to the other cases the focused power has increased, while the hotspot size is smaller.

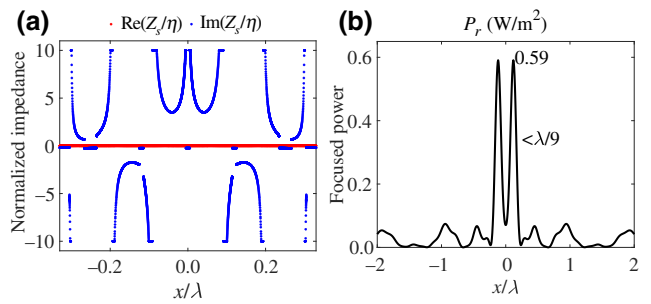


FIG. 19. Electromagnetic properties of a power flow-conformal metasurface along the  $x$ -direction at the  $z = 0$  plane for dual focusing. (a) The surface impedance along the conformal surface shows smooth changes. (b) The reflected power at the focal line  $z = 0.2\lambda$  shows focused power 0.59 ( $\text{W/m}^2$ ) and hotspot size less than  $\lambda/9$ .

## VI. CONCLUSION

Based on power flow analysis and the concept of the perfect lens, we have established a method to engineer metasurfaces for subwavelength focusing of electromagnetic waves. Compared to conventional geometrical designs such as a parabolic reflector, introduced metasurfaces are shaped along the power flow of the desired field distribution. The designed reflectors can be implemented by lossless and locally responding elements, based on reactive phase shifters. In the examples considered we have achieved subwavelength focusing with half-power spot width of the order of  $\lambda/8$ . This is not a limiting value, because it is possible to obtain even smaller hotspot sizes by involving more spatial harmonics in the definition of the reflector surface impedance. We hope that the results of this work pave the way for developing various applications that require subwavelength focusing.

## ACKNOWLEDGMENTS

This work has been supported in part by the EPSRC under Grant EP/V048937/1. F. L. acknowledges the financial support from Xi'an Jiaotong University and Shaanxi Province, P. R. China.

- [1] E. Synge, A suggested method for extending microscopic resolution into the ultra-microscopic region, *Lond. Edinb. Dublin Philos. Mag. J. Sci.* **6**, 356 (1928).
- [2] V. G. Veselago, The electrodynamics of substances with simultaneously negative values of permittivity and permeability, *Sov. Phys. Usp.* **10**, 509 (1968).
- [3] J. B. Pendry, Negative Refraction Makes a Perfect Lens, *Phys. Rev. Lett.* **85**, 3966 (2000).
- [4] A. Grbic and G. V. Eleftheriades, Overcoming the Diffraction Limit with a Planar Left-Handed Transmission-Line Lens, *Phys. Rev. Lett.* **92**, 117403 (2004).
- [5] T. Taubner, D. Korobkin, Y. Urzhumov, G. Shvets, and R. Hillenbrand, Near-field microscopy through a sic superlens, *Science* **313**, 1595 (2006).
- [6] N. Fang, H. Lee, C. Sun, and X. Zhang, Sub-diffraction-limited optical imaging with a silver superlens, *Science* **308**, 534 (2005).
- [7] D. O. S. Melville and R. J. Blaikie, Super-resolution imaging through a planar silver layer, *Opt. Express* **13**, 2127 (2005).
- [8] R. Merlin, Radiationless electromagnetic interference: Evanescent-field lenses and perfect focusing, *Science* **317**, 927 (2007).
- [9] A. Grbic and R. Merlin, Near-field focusing plates and their design, *IEEE Trans. Antennas. Propag.* **56**, 3159 (2008).
- [10] A. Grbic, L. Jiang, and R. Merlin, Near-field plates: Sub-diffraction focusing with patterned surfaces, *Science* **320**, 511 (2008).
- [11] D. Marks and P. S. Carney, Near-field diffractive elements, *Opt. Lett.* **30**, 1870 (2005).
- [12] F. M. Huang and N. I. Zheludev, Super-resolution without evanescent waves, *Nano Lett.* **9**, 1249 (2009).
- [13] E. Rogers, J. Lindberg, T. Roy, S. Savo, J. Chad, M. Dennis, and N. Zheludev, A super-oscillatory lens optical microscope for subwavelength imaging, *Nat. Mater.* **25**, 432 (2012).
- [14] G. H. Yuan, E. T. Rogers, and N. I. Zheludev, Achromatic super-oscillatory lenses with sub-wavelength focusing, *Light: Sci. Appl.* **6**, e17036 (2017).
- [15] A. Grbic, R. Merlin, E. M. Thomas, and M. F. Imani, Near-field plates: Metamaterial surfaces/arrays for subwavelength focusing and probing, *Proc. IEEE* **99**, 1806 (2011).
- [16] M. F. Imani and A. Grbic, Near-field focusing with a corrugated surface, *IEEE Antennas Wirel. Propag. Lett.* **8**, 421 (2009).
- [17] A. C. Strikwerda, T. Sleasman, W. Anderson, and R. Awadallah, Sub-wavelength focusing in inhomogeneous media with a metasurface near field plate, *Sensors* **19**, 4534 (2019).
- [18] C. L. Holloway, E. F. Kuester, J. A. Gordon, J. O'Hara, J. Booth, and D. R. Smith, An overview of the theory and applications of metasurfaces: The two-dimensional equivalents of metamaterials, *IEEE Antennas Propag. Mag.* **54**, 10 (2012).
- [19] S. B. Glybovski, S. A. Tretyakov, P. A. Belov, Y. S. Kivshar, and C. R. Simovski, Metasurfaces: From microwaves to visible, *Phys. Rep.* **634**, 1 (2016).
- [20] W. T. Chen, A. Y. Zhu, and F. Capasso, Flat optics with dispersion-engineered metasurfaces, *Nat. Rev. Mater.* **5**, 604 (2020).
- [21] O. Tsilipakos, *et al.*, Toward intelligent metasurfaces: The progress from globally tunable metasurfaces to software-defined metasurfaces with an embedded network of controllers, *Adv. Opt. Mater.* **8**, 2000783 (2020).
- [22] H. Taghvaei, A. Pitilakis, O. Tsilipakos, A. C. Tasolamprou, N. V. Kantartzis, M. Kafesaki, A. Cabellos-Aparicio, E. Alarcón, and S. Abadal, Multiwideband terahertz communications via tunable graphene-based metasurfaces in 6G networks: Graphene enables ultimate multiwideband thz waveform control, *IEEE Veh. Technol. Mag.* **17**, 16 (2022).
- [23] H. Taghvaei, On scalable, reconfigurable, and intelligent metasurfaces, UPC, Departament d'Arquitectura de Computadors (2021).
- [24] X. Luo, Subwavelength optical engineering with metasurface waves, *Adv. Opt. Mater.* **6**, 1701201 (2018).
- [25] S. Maslovski and S. Tretyakov, Phase conjugation and perfect lensing, *J. Appl. Phys.* **94**, 4241 (2003).
- [26] S. Maslovski, S. Tretyakov, and P. Alitalo, Near-field enhancement and imaging in double planar polariton-resonant structures, *J. Appl. Phys.* **96**, 1293 (2004).
- [27] S. Maslovski, P. Alitalo, and S. Tretyakov, Subwavelength imaging based on frequency scanning, *J. Appl. Phys.* **104**, 103109 (2008).
- [28] S. Maslovski and S. Tretyakov, Perfect lensing with phase-conjugating surfaces: Toward practical realization, *New J. Phys.* **14**, 035007 (2012).
- [29] L. Markley and G. V. Eleftheriades, A near-field probe for subwavelength-focused imaging, *IEEE Trans. Microw. Theory Tech.* **58**, 551 (2010).

- [30] Y. Kato and A. Sanada, Impedance-matching technique of metasurfaces generating evanescent fields for subwavelength focusing, *IEEE Trans. Microw. Theory Tech.* **68**, 1401 (2020).
- [31] M. F. Imani and A. Grbic, A unidirectional subwavelength focusing near-field plate, *J. Appl. Phys.* **115**, 044904 (2014).
- [32] M. F. Imani and A. Grbic, Unidirectional wireless power transfer using near-field plates, *J. Appl. Phys.* **117**, 184903 (2015).
- [33] O. Tereshin, V. Sedov, and A. Chaplin, *Synthesis of Antennas on Wave-Delay Structures* (Moscow, Svyaz, 1980). (in russian)
- [34] A. Díaz-Rubio, J. Li, C. Shen, S. A. Cummer, and S. A. Tretyakov, Power flow-conformal metamirrors for engineering wave reflections, *Sci. Adv.* **5**, eaau7288 (2019).
- [35] A. Díaz-Rubio and S. Tretyakov, Dual-Physics Metasurfaces for Simultaneous Manipulations of Acoustic and Electromagnetic Waves, *Phys. Rev. Appl.* **14**, 014076 (2020).
- [36] H. Taghvaee, F. Liu, A. Díaz-Rubio, and S. Tretyakov, Subwavelength focusing by engineered power-flow conformal metamirrors, *Phys. Rev. B* **104**, 235409 (2021).
- [37] G. Ma, X. Fan, F. Ma, J. de Rosny, P. Sheng, and M. Fink, Towards anti-causal Green's function for three-dimensional sub-diffraction focusing, *Nat. Phys.* **14**, 608 (2018).
- [38] G. Rosenblatt and M. Orenstein, Perfect Lensing by a Single Interface: Defying Loss and Bandwidth Limitations of Metamaterials, *Phys. Rev. Lett.* **115**, 195504 (2015).
- [39] A. Proskurin, A. Bogdanov, and D. G. Baranov, Perfect absorption of a focused light beam by a single nanoparticle, *Laser Photonics Rev.* **15**, 2000430 (2021).
- [40] J. de Rosny and M. Fink, Overcoming the Diffraction Limit in Wave Physics Using a time-Reversal Mirror and a Novel Acoustic Sink, *Phys. Rev. Lett.* **89**, 124301 (2002).
- [41] U. Leonhardt, Perfect imaging without negative refraction, *New J. Phys.* **11**, 093040 (2009).
- [42] P. Kinsler, Active drains and causality, *Phys. Rev. A* **82**, 055804 (2010).
- [43] J. C. González, P. Benítez, and J. C. Miñano, Perfect drain for the Maxwell fish eye lens, *New J. Phys.* **13**, 023038 (2011).
- [44] F. Sun, X. Ge, and S. He, Can Maxwell's fish eye lens really give perfect imaging? Part II. The case with passive drains, *Prog. Electromagn. Res. B* **110**, 313 (2010).
- [45] H. Taghvaee, F. Liu, A. Díaz-Rubio, and S. Tretyakov, in *Sixteenth International Congress on Artificial Materials for Novel Wave Phenomena (Metamaterials)* (Siena, Italy, 2022), p. X–437.
- [46] S. Tretyakov, *Analytical Modeling in Applied Electromagnetism* (Artech House, Boston, 2003).
- [47] A. Díaz-Rubio and S. A. Tretyakov, Acoustic metasurfaces for scattering-free anomalous reflection and refraction, *Phys. Rev. B* **96**, 125409 (2017).
- [48] A. Díaz-Rubio, V. S. Asadchy, A. Elsakka, and S. A. Tretyakov, From the generalized reflection law to the realization of perfect anomalous reflectors, *Sci. Adv.* **3**, e1602714 (2017).
- [49] A. Epstein and G. V. Eleftheriades, Synthesis of Passive Lossless Metasurfaces Using Auxiliary Fields for Reflectionless Beam Splitting and Perfect Reflection, *Phys. Rev. Lett.* **117**, 256103 (2016).
- [50] A. Díaz-Rubio, V. S. Asadchy, A. Elsakka, and S. A. Tretyakov, From the generalized reflection law to the realization of perfect anomalous reflectors, *Sci. Adv.* **3**, e1602714 (2017).
- [51] D. Sievenpiper, L. Zhang, R. Broas, N. Alexopolous, and E. Yablonovitch, High-impedance electromagnetic surfaces with a forbidden frequency band, *IEEE Trans. Microw. Theory Tech.* **47**, 2059 (1999).
- [52] O. Luukkonen, C. Simovski, G. Granet, G. Goussetis, D. Lioubtchenko, A. V. Raisanen, and S. A. Tretyakov, Simple and accurate analytical model of planar grids and high-impedance surfaces comprising metal strips or patches, *IEEE Trans. Antennas Propag.* **56**, 1624 (2008).
- [53] A. Harvey, Periodic and guiding structures at microwave frequencies, *IRE Trans. Microw. Theory Tech.* **8**, 30 (1960).